ACS OMEGA

Open Access

http://pubs.acs.org/journal/acsodf

Article

Engineering Porosity-Tuned Chitosan Beads: Balancing Porosity, Kinetics, and Mechanical Integrity

Astha Upadhyay,[†] Farbod Alimohammadi,[†] and Rouzbeh Tehrani*

Cite This: *ACS Omega* 2024, 9, 33857−33867

Read Online

ACCESS | Metrics & More | Article Recommendations

ABSTRACT: Chitosan, a cationic natural polysaccharide derived from the deacetylation of chitin, is known for its solubility in diluted acidic solutions, biodegradability, biocompatibility, and nontoxicity. This study introduces three innovative methods for preparing various types of porous chitosan beads: solvent extraction, surfactant extraction, and substance decomposition. These methods involve the integration and subsequent extraction or decomposition of materials during the synthesis process, eliminating the need for additional steps. We used state-of-the-art characterization techniques to analyze and evaluate the chemical and physical properties of the beads, such as Fourier-transform infrared spectroscopy (FT-IR), scanning electron microscopy (SEM), X-ray diffraction (XRD), and three-dimensional (3D) computed tomography (CT) scanning. The 3D CT scans visualized and measured the porosity of different bead types, ranging from 68.4% to 39.3%. This study also evaluated the mechanical properties of the particle beads under compressive forces in both wet and dry conditions, highlighting the influence of porosity on their mechanical integrity and compression pressure behavior. The adsorptive properties of these chitosan beads were studied using methylene blue as a model pollutant, emphasizing the importance of balancing porous structure, surface area, kinetics, and structural integrity. This study paves the way for the development of environmentally sustainable polymeric beads, highlighting the crucial need to balance porosity, surface area, and structural integrity to optimize their effectiveness in real-world applications.

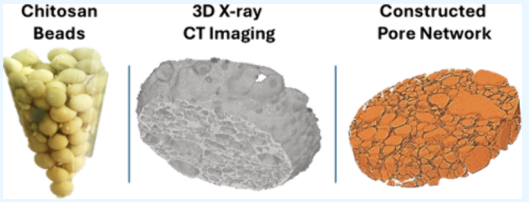

INTRODUCTION

Chitosan is a natural polysaccharide derived from the deacetylation of chitin.[1−3] Chitin is the most abundant natural polymer after cellulose.[3] The application of chitin is limited because it is insoluble in most solvents, while chitosan is soluble in diluted acidic solutions.[3] Chitosan is extensively used as a scaffold or hydrogel for various applications such as tissue engineering and drug deliveries.[3,4] Chitosan is a biodegradable, biocompatible, nontoxic, and low-cost polymer, making it an ideal candidate for industrial-scale applications.[3] Chitosan has been widely used to remove heavy metals, microorganisms, organic and inorganic compounds from wastewater[3,5−8] and can be functionalized or serve as scaffolds for embedding inorganic materials.[1,3,5−7,9−11]

Engineered porosity of the polymeric beads can play a crucial role in their efficiency in water treatment and medical applications.[1,4,5,8,12−14] Introducing porous morphology to the particles provides additional active sites and surface area for removing the pollutants or loading of drugs.[1,4,5,8,9] Various methods are introduced to prepare porous chitosan beads. They can be classified into four different strategies, including freeze-drying,[1,15,16] sol−gel,[1,17,18] phase inversion,[1,19] and using a porogen agent.[1,20] The conventional method is the freeze-drying method (also known as lyophilization), it involves the freezing of the solvent at low temperature and then removal of the solvent by sublimation under a vacuum which leads to the formation of porous structures.[1,15] However, the freeze-drying process is time-consuming and expensive, which limit its application for industrial scale. The sol−gel strategy is similar to the freeze-drying method, while the sample is not frozen and dried under supercritical conditions.[1,17,18] Phase inversion is another standard method to prepare porous polymer.[1,19] There is a solvent exchange with nonsolvent, and precipitation occurs to form a porous structure.[1,19] Another method is based on the addition of a porogen agent, which can be extracted by leaching.[1,20,21]

Controlling the size and porosity of the polymeric particles is critical in determining their physical and chemical characteristics.[4,22] Typically, chitosan beads are synthesized by dissolving chitosan polymer in dilute acetic acid, followed by the formation of a hydrogel.[23,24] Subsequently, elevating the pH of the polymer solution deprotonates the chitosan, diminishing the solubility of the polymer chains, and results in the formation of microsphere particles through van der Waals forces, hydrogen bonding, and hydrophobic interactions.[23,24] We present three distinct approaches for synthesiz-

Received: April 14, 2024
Revised: July 4, 2024
Accepted: July 11, 2024
Published: July 24, 2024

ing porous chitosan beads, each involving incorporating a material into the polymer solution, followed by its subsequent extraction or decomposition during synthesis. These approaches are classified as solvent extraction, surfactant extraction, and substance decomposition. The solvent extraction technique employs an oil-in-water (O/W) emulsification process, wherein the organic phase, specifically 2-methylpentane, is integrated into the chitosan solution (aqueous phase). Subsequently, the organic phase is removed during the synthesis procedure. In an alternative approach, a polysorbate surfactant is introduced to the polymer solution and subsequently eliminated from the polymer microsphere particles during synthesis. The final method involves the addition of azodicarbonamide to the chitosan solution, followed by its decomposition throughout the synthesis process. Notably, these processes do not require any additional steps during synthesis.

This study focuses on precisely tuning and controlling the pore structure and surface morphology to optimize their real-world application in water treatment. The structural properties of chitosan beads are studied using Fourier-transform infrared spectroscopy (FT-IR), scanning electron microscopy (SEM), and X-ray diffraction (XRD). The three-dimensional (3D) computed tomography (CT) scanning was applied to study and compare the porosity of different beads. More importantly, the structural integrity of newly introduced biopolymeric beads needs to be investigated under wet conditions, especially for large-scale water treatment. Most initial research on developing biopolymeric beads for water treatment does not extend to examining their behavior under compressive forces in wet conditions. Thus, the mechanical properties of the beads were studied under compression in wet and dry conditions.

For studying removal kinetics, methylene blue, a water-soluble dye, was used as a model contaminant. Its ease of detection and resemblance to a wide range of organic pollutants render it a common standard for assessing adsorption kinetics.[25,26] Thus, this study used methylene blue as a model contaminant to assess its removal efficiency by chitosan beads varying in porosity and morphology. In conclusion, we aimed to achieve an optimal balance among porosity, kinetics, and mechanical strength, targeting a synergistic enhancement of adsorption performance and structural integrity.

MATERIALS AND METHODS

Materials. Low molecular weight chitosan (75−85% deacetylation, and a molecular weight range: 50 000−190 000 Da), glutaraldehyde, azocarboxamide (azodicarbonamide), fluorescein isothiocyanate isomer I (90%), glacial acetic acid, sodium hydroxide, and polysorbate 20 (Tween 20) were purchased from the Sigma-Aldrich company. All chemicals were used as received without further purification.

Synthesis. Two grams of low molecular weight chitosan polymer was dissolved in 80 mL of glacial acetic acid solution (2%) at 70 °C. The obtained chitosan solution was added dropwise into a NaOH aqueous solution (1 M). The beads were aged overnight and then rinsed with DI water to obtain a neutral pH. Then, the beads were added to glutaraldehyde solution (5%) to cross-link the beads overnight. The cross-linked beads were washed with DI water and were dried at room temperature.

The porous microsphere particles (or beads) were synthesized using the same procedure but with three different additives to the chitosan solution. The first method is based on the addition of the organic phase/surfactant to the polymer solution; 10 mL of 2-methylpentane (as organic phase) and 24 mL of tween 20 (as surfactant) were mixed and then added to the polymer solution. The sample made from this method is named PCP-M. The second method is based on adding a porogen agent (4 g of azocarboxamide) to the chitosan solution. Beads made by using azocarboxamide are named PCP-A. In the last method, 35 mL of tween 20 (a porogen agent) was added to the polymer solution, the PCP-T sample. In summary, "PCP" denotes porous chitosan particles, "M" represents 2-methylpentane, "A" signifies azodicarbonamide, and "T" refers to Tween 20.

Characterization. Synthesized porous chitosan microspheres and nonporous chitosan microspheres were characterized by X-ray diffraction (XRD) using a Bruker D8 X-ray diffractometer with Cu Kα radiation (λ = 0.15406 nm), Fourier transform infrared spectroscopy (FTIR) using a PerkinElmer Spectrum 100 FT-IR spectrometer, scanning electron microscopy (SEM) using an FEI Quanta 450 FEG, and fluorescent microscopy (FM). The thermal properties of the samples were studied using thermogravimetric analysis (TGA) with a TG 209F1 Libra instrument (NETZSCH).

A Bruker D8 X-ray diffractometer with Cu Kα radiation (λ = 0.15406 nm) obtained X-ray powder diffraction patterns of tuned chitosan microspheres and nonporous chitosan microspheres. DIFFRAC.EVA software was used to determine the crystallite size of the samples. Samples were scanned from 5 to 80° (2θ value), with a 0.02° step and 0.3 s per step.

FTIR-attenuated total reflection (ATR) analysis was conducted using a PerkinElmer Spectrum 100 FT-IR spectrometer. The spectra were obtained from 400 to 4000 cm^{-1}, with 2 cm^{-1} resolution and four accumulated scans per sample (n = 5). The spectral peaks were identified using a second derivative plot, and assignments were done using available literature. The data were used to identify the functional group present in the chitosan beads synthesized using different processes.

SEM imaging was done using an FEI Quanta 450 FEG scanning electron microscope (SEM) equipped with energy-dispersive X-ray spectroscopy (SEM-EDS). The instrument was used at 5 kV, and the samples were mounted on carbon tape. Fluorescent imaging was done using an Olympus fluorescent microscope. The porous and nonporous chitosan beads were individually placed in the microscope with 1 mg/L of fluorescein isothiocyanate isomer I (90%) dye. The microscope was at 10× magnification, and different z-stack images were captured.

A high-resolution X-ray computed tomography instrument, the Rigaku Nano3DX, was used to scan the beads' 3D structure. A copper target with fields of view of 3.6 × 2.8 mm was used.

Nitrogen isotherms were performed at 77 K using an ASAP2460 instrument. The specific surface area was calculated using Brunauer, Emmett, and Teller (BET); Langmuir; and t-plot external. The total pore volumes were calculated from the amount of nitrogen adsorbed at P/P0, 0.9947, 0.9956, 0.9944, and 0.9947 for the control, PCP-M, PCP-T, and PCP-A, respectively.

Adsorption Studies. Methylene blue removal was monitored via a UV−vis spectrophotometer. The UV−vis spectra for both porous and nonporous chitosan beads were acquired at 664 nm using a DR 5000 UV−vis spectropho-

https://doi.org/10.1021/acsomega.4c03583
ACS Omega 2024, 9, 33857−33867

tometer (number of replicates, $n = 3$). Preliminary experiments were carried out at pH levels of 2, 4, and 6 to identify the optimal pH for effective adsorption, with pH 6 being chosen for subsequent adsorption studies. A calibration curve was plotted using 0.1, 0.2, 0.5,1.0, and 2.0 mg/L concentrations of methylene blue (MB) solution. The Freundlich isotherm was obtained by plotting 10, 25, 50, 100, 150, and 200 mg of chitosan microspheres in 5 mL of 2 ppm MB solution. The absorbance was recorded at 15, 30, 60, 90, 150, 210, 1440, and 2880 min. Many previous studies have extensively discussed Freundlich and Langmuir isotherms; thus, we do not explain them here.[25,26]

Adsorption Kinetics. The kinetic model describing the adsorption process for nonporous, PCP-M, PCP-T, and PCP-A was analyzed using adsorption capacity versus time data. The equations below were utilized to assess the kinetics and mechanism of adsorption:

$$\ln(q_e - q_t) = \ln q_e - k_1 t \text{ (pseudo-first-order kinetic model)}$$

$$\frac{t}{q_t} = \frac{1}{k_2 q_e^2} + \frac{t}{q_e} \text{ (pseudo-second-order kinetics model)}$$

where q_t (mmol/g) and q_e (mmol/g) denote the uptake amount at time t (min) and at equilibrium time t (min); k_1 (1/min) and k_2 (g/mmol/min) represent the rate constant of these models, respectively.[25,26]

Mechanical Properties. The synthesized nonporous and porous microspheres were tested for their mechanical properties using Caldaro position sensors (Caldaro Sadae, Japan) and the Deben Microtest tensile stage. Deben Microtest software (V6.1.51) was used to process the data, and deformation resistance was calculated from the nominal stress and strain curve. The ramping velocity during this work was 0.2 mm/min. Furthermore, the beads were soaked in water for 24 h to determine the effect of dampness on the mechanical strength. Nominal stress was calculated by dividing the force by the cross-sectional area of microspheres and a nominal strain by dividing displacement by the diameter of the SP before compression.[27] The slope in the linear region of the stress−strain curve is used to evaluate the deformation resistance of elastic material.[27] Similarly, the nominal stress and strain at the first inflection point, where the first fracture occurs, was defined as the yield strength of the material. The size of the porous beads was around 2.0−2.4 mm, and the diameter of the control beads was 1.5−1.8 mm. The analysis was repeated at least two times. The force−distance curves resulting in extremely high or low stiffness were excluded. When the tip was in contact with the substrate instead of the top of the microsphere, inaccurate high stiffness was recorded. Unacceptable low stiffness values were observed when the tip contacted the side of the microspheres, and lateral motion occurred.

RESULTS

Imaging. SEM and fluorescent images (FM) of nonporous microspheres and synthesized PCP-M, PCP-A, and PCP-T are shown in Figure 1. SEM images of the nonporous microsphere proved the absence of pores, and the FM images did not show any fluorescence due to the lack of pores. PCP-M, PCP-A, and PCP-T microspheres showed porosity in both SEM and FM images. Numerous factors, such as the quantity and variety of porogen, monomer composition, drying conditions, and cross-linking agents, can influence the pore structure.[28] The pore size of PCP-A was the largest, followed by PCP-M, while PCP-T exhibited the smallest pore size, leading to a high-density, finely porous network. Z-stack imaging of PCP-M and PCP-A microspheres revealed highly branched pores and extensive tunnel-like structures, respectively. Corresponding SEM images confirmed these structures, highlighting the distinct impacts of each porogen on the microspheres' morphology.

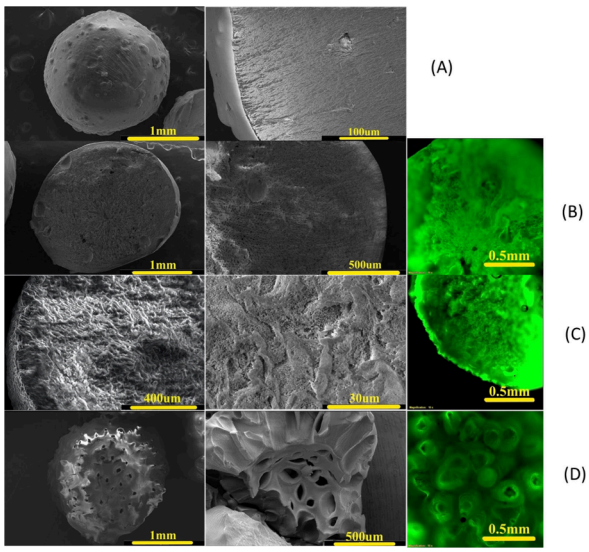

Figure 1. (A) SEM images of nonporous microspheres. SEM and FM images of (B) PCP-M, (C) PCP-T, and (D) PCP-A beads. The nonporous bead could not be observed using fluorescent microscopy, indicating that the fluorescent dye could not penetrate the particles.

Surface Area Analysis. A nitrogen adsorption−desorption experiment evaluated the beads' surface area, pore size, and pore diameter (Figure 2). According to International Union of Pure and Applied Chemistry (IUPAC) classified nitrogen adsorption−desorption isotherms, our samples show the type IV behavior with H3 hysteresis loops. Type IV isotherm appears when there is an interaction between gas molecules and adsorbent mesopore surface, leading to capillary condensation. The type IV isotherm corresponds to micro- and mesopores in the substance.

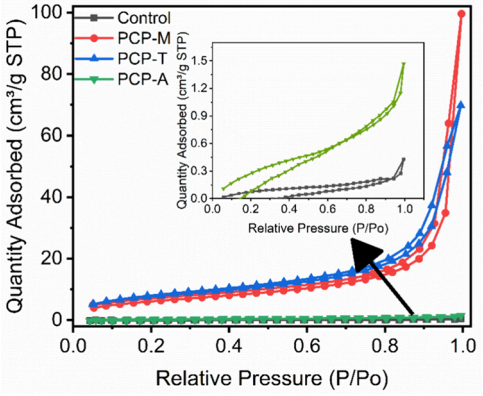

Figure 2. Nitrogen adsorption and desorption curve of the chitosan beads.

The BET, Langmuir, and t-Plot external surface area of samples arise after introducing porosity to the beads (Table 1). The surface area of the PCP-T and PCP-M are significantly

https://doi.org/10.1021/acsomega.4c03583
ACS Omega 2024, 9, 33857−33867

Table 1. Surface Area, Pore Size, and Pore Diameter of Chitosan Beads[a]

samples	BET surface area (m^2/g)	Langmuir surface area (m^2/g)	t-plot external surface area (m^2/g)	total pore volume of pores (cm^3/g)	adsorption average pore diameter (nm)	BJH adsorption average pore diameter (nm)	D−H adsorption average pore diameter (nm)
control	0.32	1.24	0.47	6.64×10^{-4}	8.28	13.06	6.92
PCP-M	21.19	111.53	23.90	0.15	28.81	30.79	9.47
PCP-T	25.76	126.71	27.59	0.11	16.77	19.66	16.07
PCP-A	1.23	6.84	1.72	2.272×10^{-3}	7.37	10.03	6.46

[a]The total pore volume and pore diameters were calculated from the N_2 adsorption isotherms.

higher than the control. Although the surface area of PCP-A is more elevated than the control, it is notably lower than PCP-M and PCP-T. SEM results confirmed that the microporous structure is more dominant in the PCP-A sample. The results suggest PCP-T shows a higher surface area and smaller pores than PCP-M.

X-ray CT Imaging. Figure 3 presents a series of X-ray CT images illustrating the cross sections of chitosan beads. The

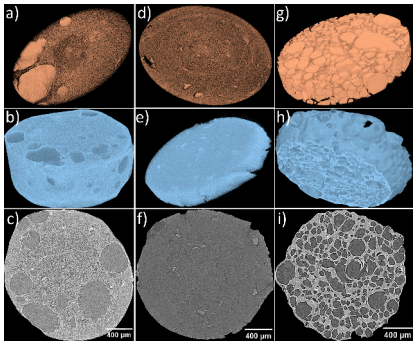

Figure 3. X-ray CT images from the cross-section of the chitosan beads: (a, b, and c) PCP-M, (d, e, and f) PCP-T, (g, h, and i) PCP-A. The 3D images of the pores at the top, the 3D images of the beads at the middle, and 2D single slice images at the bottom. The image analysis showed 68.4%, 39.3%, and 65.0% porosity for the PCP-M, PCP-T, and PCP-A, respectively.

images are categorized into three sets: PCP-M, PCP-T, and PCP-A. Each set comprises three images: a 3D pore image at the top, a 3D bead image in the middle, and a 2D single slice image at the bottom. The 3D pore images vividly display the porous architecture of the beads, allowing for a clear visualization of the interconnected porosity within the chitosan beads. The 3D bead images provide a comprehensive view of the beads' morphology, offering insights into their structural integrity and overall form. Meanwhile, the 2D single-slice images provide a detailed view of the internal structure of the beads, enabling a closer examination of the pore distribution and wall thickness.

Quantitative image analysis revealed variances in the porosity of the beads, with the PCP-M beads exhibiting a porosity of 68.4%, followed by the PCP-A beads at 65.0%, and the PCP-T beads showing the lowest porosity at 39.3%. This quantitative data, in conjunction with the visual insights from the images, allows for an understanding of the structural characteristics and porosity of the chitosan beads. PCP-M beads are highly porous with a moderate surface area, making them suitable for applications requiring substantial internal spaces, such as drug encapsulation or delivery. On the other hand, PCP-A shows a high porosity but significantly lower surface area. These beads might be limited in applications requiring substantial surface interactions but could still be useful in applications necessitating internal carrying capacities, such as controlled release of substances.

X-ray Diffraction (XRD) Analysis. XRD patterns of the powdered, synthesized, nonporous, and porous chitosan microspheres were obtained to determine the crystalline structure (Figure 4). From the pattern, the two characteristic peaks at 10° and 20° of the extracted chitosan with a crystalline structure. Powdered pristine chitosan had an intense peak at 20° with a sharp peak corresponding to the chitosan phase. Similar peaks of the chitosan phase were observed in synthesized chitosan. The crystallinity and crystallite size of the chitosan beads are shown in Figure 4b. The crystallite size of the beads decreased by introducing porosity to the structure and was calculated using the peak at 20°, and they are in the range of 20−45 Å. However, crystallinity slightly increases with the introduction of porosity. Overall, the changes are very slim, with no significant differences noted.

FTIR and TGA Analysis. In Figure 5, we can observe the infrared spectrum of chitosan. A strong band in the region 3291−3361 cm^{-1} corresponds to N−H and O−H stretching, as well as the intramolecular hydrogen bonds. The absorption

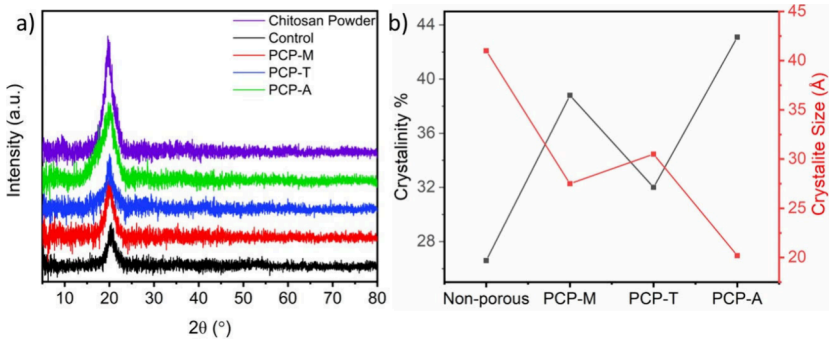

Figure 4. (a) XRD diffractogram of nonporous chitosan beads, fine-tuned chitosan beads, namely, PCP-M, PCP-T, and PCP-A, and powdered chitosan. (b) Crystallinity and crystallite size of the chitosan beads.

https://doi.org/10.1021/acsomega.4c03583
ACS Omega 2024, 9, 33857−33867

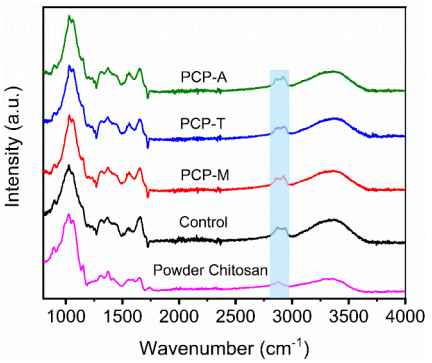

Figure 5. FTIR spectra of the porous chitosan beads and powdered chitosan.

bands at around 2921 and 2877 cm^{-1} can be attributed to C−H symmetric and asymmetric stretching, respectively. These bands are characteristics typical of polysaccharides and are found in other polysaccharide spectra, such as xylan, glucans, and carrageenan. The powder chitosan and PCP-M peak around 2921 and 2877 cm^{-1} had lower intensity, indicating similar stretching, whereas PCP-A and PCP-T had higher intensity bands. The presence of residual-acetyl groups was confirmed by the bands around 1645 cm^{-1} (C═O stretching of amide I) and 1325 cm^{-1} (C−N stretching of amide III), respectively. The band corresponding to the N−H bending of amide II was missing at 1550 cm^{-1} in powder chitosan, indicating possible overlap with other bands, but a small band was observed in the synthesized porous samples. The 1423 and 1375 cm^{-1} bands confirm the CH_2 bending and CH_3 symmetrical deformations, respectively. The absorption bands at 1153 cm^{-1} and 1066 and 1028 cm^{-1} can be attributed to the asymmetric stretching of the C−O−C bridge and C−O stretching, respectively. All bands are found in the spectra of samples of chitosan reported previously.[29]

The TGA curves of chitosan beads exhibit weight loss in three stages, as shown in Figure 6. The first stage appeared in the 40−100 °C range, which can be attributed to the water loss. The water weight loss is around 0.9% for the control sample, while it is significantly higher for the porous beads, around 6−11%. The second degradation is around 280 °C. A change of the thermogram curve at 430 °C suggests a slower third process. Another process was observed in the derivative curve between 550 and 650 °C. The correspondent derivative curve reached zero between 650 and 800 °C with no evident distinct events. The FTIR analysis conducted on the samples previously demonstrated the presence of specific peaks corresponding to certain functional groups.

Previous research has reported that evolved gas mainly composed of H_2O, NH_3, CO, CO_2, CH_3COOH, and CH_4 is released during the degradation of chitosan.[28,30,31] A main process involving the release of H_2O, NH_3, CO, CO_2, and CH_3COOH is assigned to the pyrolytic degradation of chitosan and assessed in the literature in the temperature range 250−450 °C.[28,30,31] In the temperature range of 225−450 °C, a weight loss of ∼55 wt % was observed, possibly corresponding to this gaseous release. At lower temperatures, NH_3 release is initiated, which reaches its peak at 325 °C, suggesting a low activation energy for NH_3 formation. A second process characterized by the release of CH_4 possibly happened in the range 550−650 °C, corresponding to a loss of ∼31 wt %. The highest rate of CH_4 generation is observed at around 590 °C in control chitosan, as observed in the previous studies.[1,28,30,31] The synthesized microspheres have a deviation in the peak between 550 and 650 °C, with the maximum generation of CH_4 observed around 550, 580, and 650 °C for PCP-M, PCP-T, and PCP-A, respectively. A modification of the material is suspected after the complete reduction of the structure, causing methane production and the consequent formation of a graphite-like structure via a dehydrogenation mechanism, as suggested in the literature.[28,30,31] Monitoring the evolution of species in temperature/time scale is imperative to identify a complex degradation pattern.

The thermal stability of chitosan beads in the 300−700 °C range is inversely related to their surface area and porosity. PCP-M, synthesized with 2-methylpentane and Tween 20, has a high surface area and highest porosity, resulting in more active sites for thermal degradation and thus reduced thermal stability. In contrast, PCP-A, made with azodicarbonamide, has high porosity, bigger and more uniform pores, and the lowest surface area, leading to fewer active sites for degradation and greater thermal stability. TGA analysis confirms that higher porosity and surface area accelerate thermal decomposition.

Mechanical Analysis. The mechanical properties of the microspheres were obtained by analyzing the force−distance curves centered on the bead. Figure 7 shows the setup of the beads in the MicroTesting unit. Finally, four curves for the synthesized porous and nonporous microspheres of each size were used to plot stress and strain.

During the compression, the shape of the beads changes continuously. Therefore, we use nominal stress and strain instead of stress and strain.[27] The nominal stress (calculated by the applied force divided by the cross-sectional, as a function of

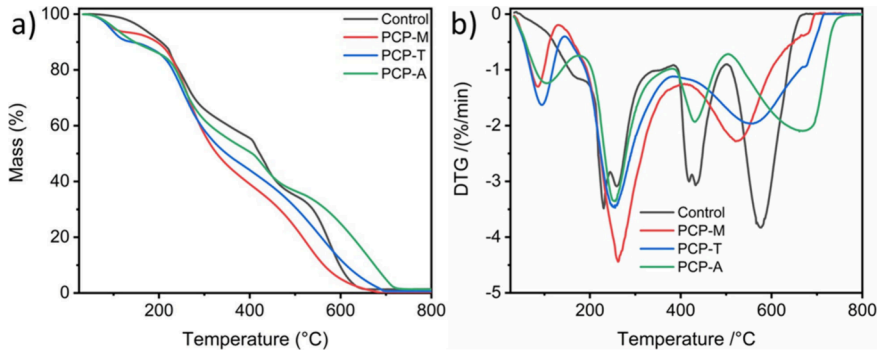

Figure 6. Results from (a) thermogravimetric analysis of the chitosan beads and (b) derivative thermogravimetry of chitosan beads.

https://doi.org/10.1021/acsomega.4c03583
ACS Omega 2024, 9, 33857−33867

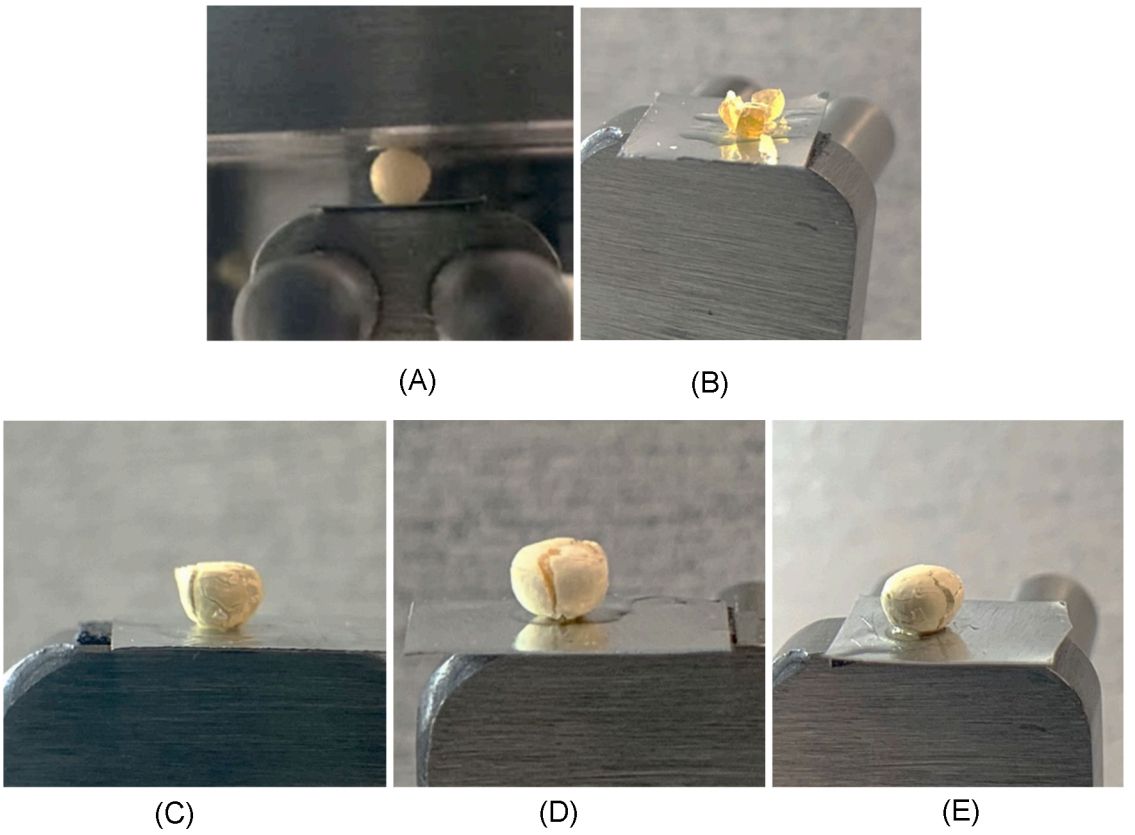

Figure 7. (A) In situ microtesting experimental setup. Photos taken after material failure: (B) nonporous bead, (C) PCP-M, (D) PCP-A, and (E) PCP-T beads.

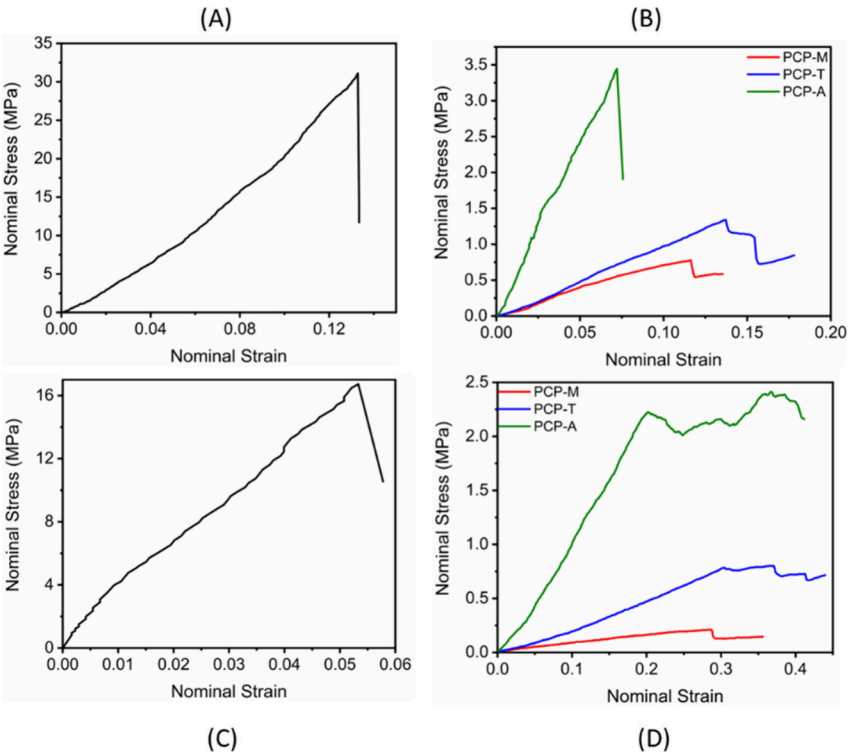

Figure 8. Nominal stress and strain graph from the in situ microtesting of the (A) nonporous; (B) PCP-M, PCP-A, and PCP-T beads; (C) soaked nonporous; and (D) soaked PCP-M, PCP-A, and PCP-T beads.

https://doi.org/10.1021/acsomega.4c03583
ACS Omega 2024, 9, 33857−33867

Table 2. Comparative Summary of Deformation Resistance and Compressive Strength of the Microspheres before and after 24 h of Soaking in Water

	deformation resistance (MPa)		compressive strength (MPa)	
microsphere	nonsoaked	soaked	nonsoaked	soaked
nonporous	235.4 ± 11.3	304.1 ± 36.3	31.6 ± 0.6	19.9 ± 4.5
PCP-M	7.9 ± 0.7	0.7 ± 0.0	0.8 ± 0.0	0.2 ± 0.0
PCP-T	10.0 ± 0.2	2.6 ± 0.2	1.3 ± 0.1	0.8 ± 0.1
PCP-A	40.9 ± 23.8	15.7 ± 5.1	3.5 ± 0.1	2.3 ± 0.4

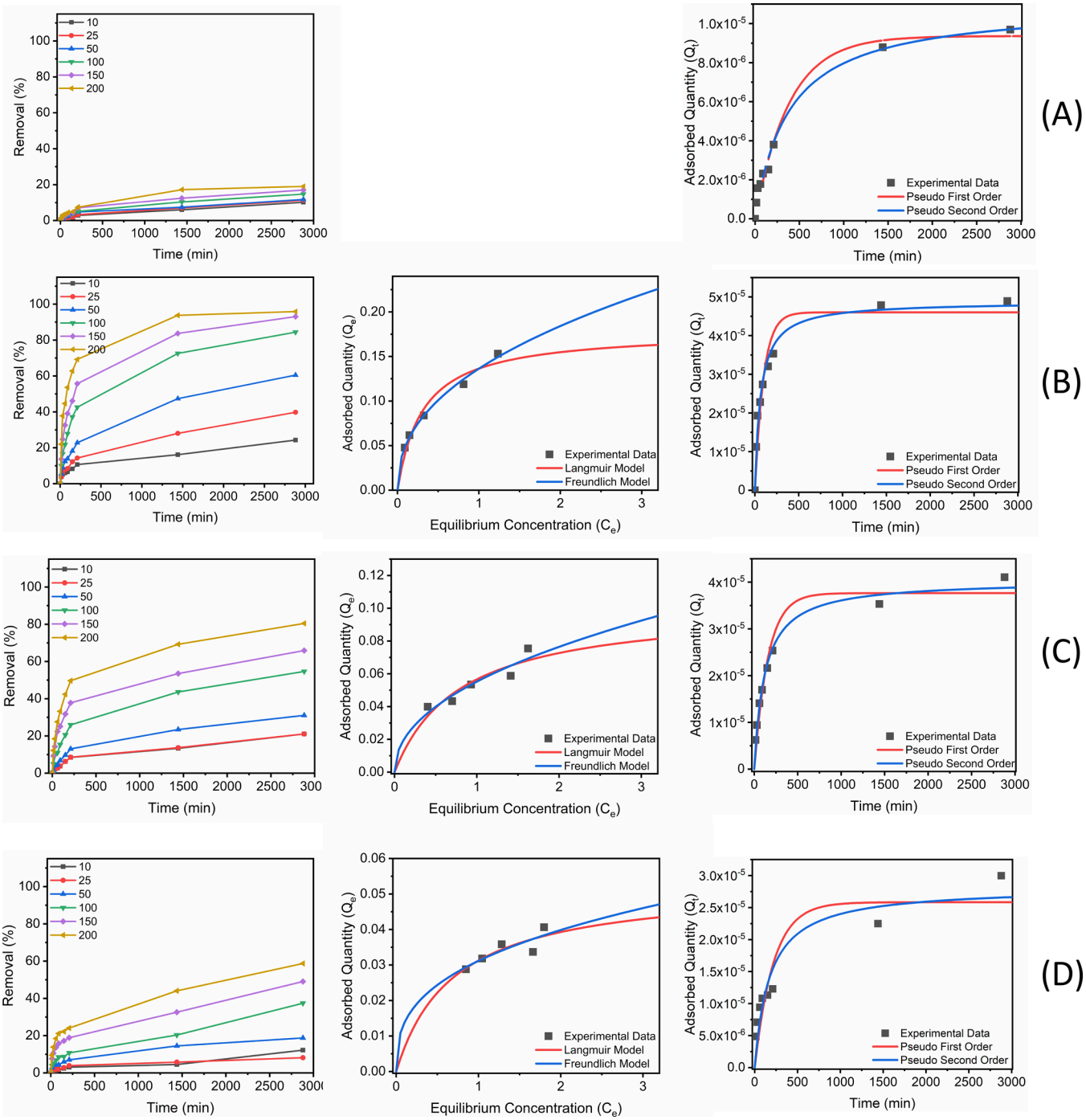

Figure 9. Removal rate, adsorption isotherms, and adsorption kinetics of (A) nonporous, (B) PCP-M, (C) PCP-T, and (D) PCP-A. The left column depicts the removal rate (%) over time. The middle column depicts Langmuir and Freundlich isotherms, and the right column depicts pseudo-first- and pseudo-second-order kinetics.

https://doi.org/10.1021/acsomega.4c03583
ACS Omega 2024, 9, 33857−33867

nominal strain (the displacement divided by the diameter of beads) was measured to assess the elastic properties of the chitosan microspheres.

Young's modulus is determined based on uniaxial tension or compression. To measure Young's modulus of a bead, we need to determine the effective modulus of the bead using the equation below:

$$F = E^* \sqrt{r \times \delta^{3/2}} \quad (1)$$

F, d, and δ are applied force, bead diameter, and total displacement.[27,32−34] Young's modulus can be calculated from the effective modulus:[32−34]

$$E^* = \frac{E}{1 - \nu^2} \quad (2)$$

ν is the position ratio of the beads. The Poisson ratio of our beads is unknown. Therefore, we determined the slope of the nominal stress and strain as deformation resistance. Deformation resistance is equivalent to the Young modulus and can be considered an inherent property of the materials.

Figure 8 presents the stress vs strain plot to determine the synthesized material's deformation resistance (DR). The chitosan microspheres' material properties, morphology, and roughness influence the deformation resistance determined from the slope of the stress versus strain plot. Table 2 summarizes the deformation resistance and yield strength of the microspheres, and the linear part of the nominal stress and strain slope was used to determine the deformation resistance. The nonporous chitosan microspheres had the highest compressive strength (31.6 ± 0.6 MPa) and deformation resistance (235.4 ± 11.3 MPa), indicating deficient elasticity under dry conditions. PCP-M demonstrated the highest elasticity with a DR of 7.9 ± 0.7 MPa, followed by PCP-T (10.0 ± 0.2 MPa). PCP-A had the lowest elasticity and highest YM of 40.9 ± 23.8 MPa among the porous chitosan microspheres. After soaking the microsphere in water for 24 h, the elasticity of the beads changed significantly. The deformation resistance of PCP-M (0.7 ± 0.0) was the lowest, followed by PCP-T (2.6 ± 0.2 MPa) and PCP-A (15.7 ± 5.1 MPa). The elasticity of PCP-M is the lowest number in wet and dry conditions, which confirms that the beads are softer after introducing the porosity to the structure. Interestingly, the deformation resistance of the nonporous microsphere did not change drastically from nonsoaked beads (304.1 ± 36.3 MPa).

Adsorption Isotherm and Adsorption Kinetics. As shown in Figure 9, the methylene blue removal in samples was significant in synthesized porous microspheres compared to the nonporous microsphere. The uptake in porous microspheres increased with time before reaching equilibrium. The removal exceeded 90% at the equilibrium value after 1440 min, rapidly increasing after the initial 120 min, indicating fast adsorption. The nonporous microspheres showed the lowest equilibrium removal, possibly due to decreased accessibility for mass diffusion and lack of a porous network. PCP-M showed the highest q_e and k_2, consistent with its high uptake and removal rate (Table 3).

The isotherms were derived using the Freundlich and Langmuir models. The isotherm plots of the Freundlich and Langmuir models are shown in Figure 9. The Freundlich model fitted the data better, with higher correlation coefficients, indicating that the dye removal followed reversible multilayer adsorption by the heterogeneous surface of the microsphere. Furthermore, the Freundlich equation predicts that the dye concentrations on the adsorbent will increase with an increase in the dye concentration in the liquid phase.[35]

Table 3. Adsorption Isotherm of Synthesized Porous and Nonporous Chitosan Beads

	Freundlich isotherm		
sample	k	n	R^2
nonporous	4.436×10^{-8}	0.095	0.98
PCP-M	1.361×10^{-4}	2.41	0.99
PCP-T	1.039	13.66	0.93
PCP-A	3.273×10^{-5}	2.60	0.87

We examined the kinetics governing the adsorption process of the beads. The pseudo-first-order and the pseudo-second-order kinetic models were applied to analyze the adsorption kinetics. The pseudo-second-order kinetic model was more suitable for the overall adsorption process (after 2880 min), with higher correlation coefficients than those of the pseudo-first-order kinetic model, indicating the primary mechanism of chemical adsorption. The fitted curves by this model are shown in Figure 9. The PCP-M beads showed a higher equilibrium removal q_e and a lower rate constant k, possibly due to improved accessibility for mass diffusion.

DISCUSSION AND CONCLUSION

This study introduced three novel synthesis methods that provide porosity and elasticity to chitosan polymeric beads while maintaining structural integrity. These methods uniquely create tuned hollow-sphere microstructures without the need for freeze, dry, or vacuum steps, offering a novel approach in the field. The beads exhibit high porosity and maintain a relatively spherical shape without showing shrinkage or irregular morphology. Chitosan beads were rendered porous using surfactant and porogen additives using the following methods. The first method, solvent extraction utilizing oil-in-water (O/W) emulsification, was applied as the first step. The second method incorporated a polysorbate surfactant into the chitosan solution, which was later removed during synthesis and purification. The third method involved the addition of azodicarbonamide to the chitosan solution, which decomposed during the process. Most studies focus on the thermal decomposition of azodicarbonamide to introduce porosity to the structure.[36−39] Our study, however, revealed that the decomposition of azodicarbonamide occurred during the synthesis process, likely due to the treatment with a strong base, without heating the samples.

The average particle size of the nonporous chitosan, our control, was 1.7 ± 0.3 mm. In contrast, the average sizes for the porous chitosan beads were 2.2 ± 0.6 mm for PCP-M, 2.0 ± 0.3 mm for PCP-T, and 2.3 ± 0.4 mm for PCP-A. The increase in particle size of the porous chitosan beads can be attributed to several factors in the synthesis process. Incorporating additives such as 2-methylpentane, Tween 20, and azodicarbonamide increases the initial volume and mass of the chitosan droplets before gelation. These additives facilitate pore formation, either through gas evolution or the creation of emulsion droplets, which leads to an expansion of the beads. Additionally, the beads' porous structure allows for greater water absorption during the washing and cross-linking stages, causing further swelling and enlargement. Furthermore, surfactants and other additives alter the surface tension and

https://doi.org/10.1021/acsomega.4c03583
ACS Omega 2024, 9, 33857−33867

viscosity of the droplets during formation. Consequently, combining these factors results in porous chitosan beads with significantly larger particle sizes than nonporous chitosan beads. FTIR and XRD analyses confirmed the presence of the chitosan phase and identified structural similarities and deviations compared to powdered chitosan. The FTIR spectrum of chitosan showed prominent bands attributed to the stretching vibrations of N−H and O−H bonds and intramolecular hydrogen bonds, typical for chitosan.[29] Variations in band intensity among the different samples suggested differences in their structural or conformational properties. Additionally, the crystallinity remains almost the same, with a slight increase observed due to the introduction of porosity.

SEM, fluorescent imaging, and X-ray CT imaging elucidated the porous network within the synthesized microspheres, contrasting with the absence of such a network in nonporous chitosan. Significant variations in pore sizes among the PCP-A, PCP-M, and PCP-T samples were observed, influencing their properties. X-ray CT imaging, supplemented by SEM and fluorescent imaging, helps determine the suitability of each particle type for specific applications, from water treatment to drug delivery. The optimum pore size and highest porosity of PCP-M allow higher and faster adsorption, better elasticity, and structural integrity.[28,32]

The thermal stability of porous chitosan particle beads is closely related to their surface area and porosity, as shown by TGA, BET, and X-ray CT imaging results. CT images reveal that PCP-M has the highest porosity, followed by PCP-A and PCP-T. This high porosity and large surface area in PCP-M provide more active sites for thermal degradation, reducing thermal stability. TGA analysis (in the range of 300−700 °C) shows that PCP-M degrades faster due to its extensive surface area and porous network, facilitating an earlier onset of decomposition processes. In contrast, despite having a high porosity, PCP-A exhibits a comparatively lower surface area, resulting in fewer active sites for degradation and greater thermal stability. PCP-T, with the lowest porosity, and high surface area, demonstrates moderate thermal stability among the samples. These findings highlight that the increased porosity and surface area observed in CT images and BET data correlate with decreased thermal stability due to enhanced thermal degradation sites, emphasizing the inverse relationship between porosity and thermal stability in these porous chitosan beads. In other words, controlled pore size and volume are essential parameters in designing chitosan-based materials with tailored thermal properties for specific applications.

A complex degradation process was reported during the pyrolytic decomposition of chitosan, releasing various gases.[28,30,31] In control chitosan, the peak CH_4 generation is observed at approximately 590 °C.[28,30,31] However, deviations in this peak were noted for PCP samples. These variations suggest structural modifications in the synthesized microspheres. This process may contribute to the formation of a graphite-like structure, which is advantageous for applications requiring high thermal stability and electrical conductivity.[28,30,31]

Porous structures offer benefits over bulk and nonporous samples, yet it is crucial for these porous beads to maintain their structural integrity under both dry and wet conditions to leverage these advantages. As our study confirms, the introduction of porosity significantly reduces the compressive strength of the beads. Nonporous chitosan exhibited the highest compressive strength, attributable to its dense pack morphology, but did not achieve optimum contaminant removal. This finding underscores the importance of optimizing the balance between structural integrity and the rates and capacities of contaminant removal when synthesizing chitosan beads, or more broadly any biopolymeric beads for water treatment. It is important to remember that polymers exhibit different behaviors under compressive stress depending on whether they are in a dry or wet state. Our recommendations for future research extend beyond analyzing the behavior of beads in their wet state, as demonstrated in this study, and include an assessment of the shelf life of biopolymeric beads. This evaluation is crucial to ascertaining whether their structural integrity alters over time, a key factor in their long-term effectiveness in water treatment applications.

In conclusion, our integrated approach using multiple analytical techniques confirmed the physical properties and structural differences between chitosan and synthesized porous chitosan beads. These findings not only provide a comprehensive understanding of chitosan's structural and functional properties but also open a new window for its optimization in various applications. For instance, PCP-M's high porosity and surface area make it ideal for applications needing large internal spaces, such as drug encapsulation or delivery. Conversely, while PCP-A has high porosity, its lower surface area may limit its effectiveness in applications requiring extensive surface interactions, but it remains suitable for uses like controlled substance release. These potential applications motivate further research to explore the capabilities of porous chitosan beads and refine their synthesis methods.

AUTHOR INFORMATION

Corresponding Author

Rouzbeh Tehrani − *Department of Civil and Environmental Engineering, Temple University, Philadelphia, Pennsylvania 19122, United States;* orcid.org/0000-0002-5989-7049; Email: r.tehrani@temple.edu

Authors

Astha Upadhyay − *Department of Civil and Environmental Engineering, Temple University, Philadelphia, Pennsylvania 19122, United States;* orcid.org/0000-0002-7608-2191

Farbod Alimohammadi − *Department of Civil and Environmental Engineering, Temple University, Philadelphia, Pennsylvania 19122, United States;* orcid.org/0000-0002-5143-2933

Complete contact information is available at: https://pubs.acs.org/10.1021/acsomega.4c03583

Author Contributions

†These authors contributed equally to this work and share the first authorship.

Notes

The authors declare no competing financial interest.

ACKNOWLEDGMENTS

The authors express their gratitude to Dr. Dmitriy Dikin for granting access to mechanical testing instruments, Dr. Bojana Gligorijevic for providing access to the fluorescence microscope, and Dr. Steven Chemtob for the use of the XRD instrument, all from Temple University. Additionally, the authors would like to thank Dr. Josh Gibson from the Beckman

https://doi.org/10.1021/acsomega.4c03583
ACS Omega 2024, 9, 33857−33867

Institute for Advanced Science and Technology for his invaluable assistance with CT scan imaging. We gratefully acknowledge Dr. Lewis S. Rowles for his collaboration in proofreading our manuscript and conducting separate analyses on life cycle and techno-economic aspects.

REFERENCES

(1) Grzybek, P.; Jakubski, L.; Dudek, G. Neat Chitosan Porous Materials: A Review of Preparation, Structure Characterization and Application. *Int. J. Mol. Sci.* **2022**, *23* (17), 9932.
(2) Misra, S. K.; Pathak, K. Microscale and nanoscale chitosan-based particles for biomedical use. *Chitosan in Biomedical Applications* **2022**, 37.
(3) Muxika, A.; Etxabide, A.; Uranga, J.; Guerrero, P.; de la Caba, K. Chitosan as a bioactive polymer: Processing, properties and applications. *Int. J. Biol. Macromol.* **2017**, *105* (Pt 2), 1358−1368.
(4) Mi, F. L.; Shyu, S. S.; Chen, C. T.; Schoung, J. Y. Porous chitosan microsphere for controlling the antigen release of Newcastle disease vaccine: preparation of antigen-adsorbed microsphere and in vitro release. *Biomaterials* **1999**, *20* (17), 1603−1612.
(5) Wang, K.; Ma, H.; Pu, S.; Yan, C.; Wang, M.; Yu, J.; Wang, X.; Chu, W.; Zinchenko, A. Hybrid porous magnetic bentonite-chitosan beads for selective removal of radioactive cesium in water. *J. Hazard Mater.* **2019**, *362*, 160−169.
(6) Gomaa, H.; Abd El-Monaem, E. M.; Eltaweil, A. S.; Omer, A. M. Efficient removal of noxious methylene blue and crystal violet dyes at neutral conditions by reusable montmorillonite/NiFe(2)O(4)@amine-functionalized chitosan composite. *Sci. Rep* **2022**, *12* (1), 15499.
(7) Vázquez, M. O.; Ramírez-Arreola, D. E.; Bernache, J.; Gómez, C.; Robledo-Ortiz, J. R.; Rodrigue, D.; González-Núñez, R. Using Chitosan as a Nucleation Agent in Thermoplastic Foams for Heavy Metal Adsorption. *Macromol. Symp.* **2009**, *283*−*284* (1), 152−158.
(8) Rorrer, G. L.; Hsien, T. Y.; Way, J. D. Synthesis of porous-magnetic chitosan beads for removal of cadmium ions from wastewater. *Ind. Eng. Chem. Res.* **1993**, *32* (9), 2170−2178.
(9) Zhao, H.; Xu, J.; Lan, W.; Wang, T.; Luo, G. Microfluidic production of porous chitosan/silica hybrid microspheres and its Cu(II) adsorption performance. *Chemical Engineering Journal* **2013**, *229*, 82−89.
(10) Tu, N.; Shou, J.; Dong, H.; Huang, J.; Li, Y. Improved Catalytic Performance of Lipase Supported on Clay/Chitosan Composite Beads. *Catalysts* **2017**, *7* (10), 302.
(11) Wang, M.; Ma, Y.; Sun, Y.; Hong, S. Y.; Lee, S. K.; Yoon, B.; Chen, L.; Ci, L.; Nam, J. D.; Chen, X.; et al. Hierarchical Porous Chitosan Sponges as Robust and Recyclable Adsorbents for Anionic Dye Adsorption. *Sci. Rep* **2017**, *7* (1), 18054.
(12) Dai, C.; Li, Y.; Pan, W.; Wang, G.; Huang, R.; Bu, Y.; Liao, X.; Guo, K.; Gao, F. Three-Dimensional High-Porosity Chitosan/Honeycomb Porous Carbon/Hydroxyapatite Scaffold with Enhanced Osteoinductivity for Bone Regeneration. *ACS Biomater Sci. Eng.* **2020**, *6* (1), 575−586.
(13) Jana, S.; Florczyk, S. J.; Leung, M.; Zhang, M. High-strength pristine porous chitosan scaffolds for tissue engineering. *J. Mater. Chem.* **2012**, *22* (13), 6291.
(14) Huang, L.; Xiao, L.; Jung Poudel, A.; Li, J.; Zhou, P.; Gauthier, M.; Liu, H.; Wu, Z.; Yang, G. Porous chitosan microspheres as microcarriers for 3D cell culture. *Carbohydr. Polym.* **2018**, *202*, 611−620.
(15) Qian, L.; Zhang, H. Controlled freezing and freeze drying: a versatile route for porous and micro-/nano-structured materials. *J. Chem. Technol. Biotechnol.* **2011**, *86* (2), 172−184.
(16) Ren, L.; Xu, J.; Zhang, Y.; Zhou, J.; Chen, D.; Chang, Z. Preparation and characterization of porous chitosan microspheres and adsorption performance for hexavalent chromium. *Int. J. Biol. Macromol.* **2019**, *135*, 898−906.
(17) Maleki, H.; Duraes, L.; Garcia-Gonzalez, C. A.; Del Gaudio, P.; Portugal, A.; Mahmoudi, M. Synthesis and biomedical applications of aerogels: Possibilities and challenges. *Adv. Colloid Interface Sci.* **2016**, *236*, 1−27.
(18) Pandis, C.; Madeira, S.; Matos, J.; Kyritsis, A.; Mano, J. F.; Ribelles, J. L. Chitosan-silica hybrid porous membranes. *Mater. Sci. Eng. C Mater. Biol. Appl.* **2014**, *42*, 553−561.
(19) Li, J.; Wu, X.; Wu, Y.; Tang, Z.; Sun, X.; Pan, M.; Chen, Y.; Li, J.; Xiao, R.; Wang, Z.; et al. Porous chitosan microspheres for application as quick in vitro and in vivo hemostat. *Mater. Sci. Eng. C Mater. Biol. Appl.* **2017**, *77*, 411−419.
(20) Bharadwaz, A.; Jayasuriya, A. C. Fabrication of porous chitosan particles using a novel two-step porogen leaching and lyophilization method with the label-free multivariate spectral assessment of live adhered cells. *Colloids Surf. B Biointerfaces* **2021**, *208*, 112094.
(21) Liu, Y.; Cai, Z.; Jin, Y.; Sheng, L.; Ma, M. Volcanic Rock-Inspired Fabrication of Porous Chitosan Macroparticles via Gas Porogen for Enhancing the Activity of Immobilized Enzymes. *ACS Sustainable Chem. Eng.* **2020**, *8* (41), 15560−15572.
(22) Xu, J. H.; Zhao, H.; Lan, W. J.; Luo, G. S. A novel microfluidic approach for monodispersed chitosan microspheres with controllable structures. *Adv. Healthc Mater.* **2012**, *1* (1), 106−111.
(23) Yang, Y.; Chen, G.; Murray, P.; Zhang, H. Porous chitosan by crosslinking with tricarboxylic acid and tuneable release. *SN Applied Sciences* **2020**, *2* (3), DOI: 10.1007/s42452-020-2252-z.
(24) Mahaninia, M. H.; Wilson, L. D. Cross-linked chitosan beads for phosphate removal from aqueous solution. *J. Appl. Polym. Sci.* **2016**, *133* (5), 42949.
(25) Giraldo, S.; Robles, I.; Godinez, L. A.; Acelas, N.; Florez, E. Experimental and Theoretical Insights on Methylene Blue Removal from Wastewater Using an Adsorbent Obtained from the Residues of the Orange Industry. *Molecules* **2021**, *26* (15), 4555.
(26) Oladoye, P. O.; Ajiboye, T. O.; Omotola, E. O.; Oyewola, O. J. Methylene blue dye: Toxicity and potential elimination technology from wastewater. *Results in Engineering* **2022**, *16*, 100678.
(27) Wang, J.; Schwenger, J.; Strobel, A.; Feldner, P.; Herre, P.; Romeis, S.; Peukert, W.; Merle, B.; Vogel, N. Mechanics of colloidal supraparticles under compression. *Sci. Adv.* **2021**, *7* (42), No. eabj0954.
(28) Liu, W.; Zhang, Y.; Wang, S.; Bai, L.; Deng, Y.; Tao, J. Effect of Pore Size Distribution and Amination on Adsorption Capacities of Polymeric Adsorbents. *Molecules* **2021**, *26* (17), 5267.
(29) Fernandes Queiroz, M.; Melo, K. R.; Sabry, D. A.; Sassaki, G. L.; Rocha, H. A. Does the use of chitosan contribute to oxalate kidney stone formation? *Mar Drugs* **2015**, *13* (1), 141−158.
(30) Zeng, L.; Qin, C.; Wang, L.; Li, W. Volatile compounds formed from the pyrolysis of chitosan. *Carbohydr. Polym.* **2011**, *83* (4), 1553−1557.
(31) Debritto, D.; Campana-Filho, S. P. A. A kinetic study on the thermal degradation of N,N,N-trimethylchitosan. *Polym. Degrad. Stab.* **2004**, *84* (2), 353−361.
(32) Wang, L. G.; Li, Z.; Zhang, L.; Zhou, R.; Chen, X. On the Measurement of Particle Contact Curvature and Young's Modulus Using X-ray μCT. *Applied Sciences* **2021**, *11* (4), 1752.
(33) Silva, N. V.; Angulo, S. C.; da Silva Ramos Barboza, A.; Lange, D. A.; Tavares, L. M. Improved method to measure the strength and elastic modulus of single aggregate particles. *Materials and Structures* **2019**, *52* (4), DOI: 10.1617/s11527-019-1380-7.
(34) Russell, A.; Schmelzer, J.; Müller, P.; Krüger, M.; Tomas, J. Mechanical properties and failure probability of compact agglomerates. *Powder Technol.* **2015**, *286*, 546−556.
(35) Wong, Y. C.; Szeto, Y. S.; Cheung, W. H.; McKay, G. Adsorption of acid dyes on chitosan—equilibrium isotherm analyses. *Process Biochemistry* **2004**, *39* (6), 695−704.
(36) Prakash, A. S.; Swam, W. A.; Strachan, A. N. The thermal decomposition of azodicarbonamide (1,1′-azobisformamide). *J. Chem. Soc., Perkin Trans.* **1975**, *2* (1), 46−50.
(37) Bhatti, A. S.; Dollimore, D.; Goddard, R. J.; O'Donnell, G. The thermal decomposition of azodicarbonamide. *Thermochim. Acta* **1984**, *76* (1−2), 63−77.

https://doi.org/10.1021/acsomega.4c03583
ACS Omega 2024, 9, 33857−33867

(38) Jaafar, H. A. S.; Sims, G. L. A. The Thermal Decomposition of Azodicarbonamide (ADC). *Cellular Polymers* **1993**, *12* (4), 303−316.
(39) Krutko, I.; Danylo, I.; Kaulin, V. Kinetics of azodicarbonamide decomposition in the presence of an initiator for obtaining solid foams. *Voprosy Khimii i Khimicheskoi Tekhnologii* **2019**, No. 1, 26−34.

https://doi.org/10.1021/acsomega.4c03583
ACS Omega 2024, 9, 33857−33867